

Erosion Behaviors of Gas–Solid Flow on an Assignment Plate using CFD–DEM

S. Q. Gao¹, H. Z. Jin^{1†} and G. F. Ou²

¹ Faculty of Mechanical Engineering & Automation, Zhejiang Sci-Tech University, Hangzhou, Zhejiang, 310018, China

² School of Mechanical Engineering & Rail Transit, Changzhou University, Changzhou, Jiangsu, 213000, China

†Corresponding Author Email: haozhe2007@163.com

(Received November 27, 2021; accepted May 16, 2022)

ABSTRACT

The erosion wear of a gas–solid flow is a major challenge for an S Zorb reactor; it affects the production safety and stability. This study aims to investigate the erosion wear problem of a gas–solid flow on an assignment plate in an S Zorb reactor using CFD–DEM. The erosion wear behavior of the assignment plate is studied through flow field and particle trajectory analyses. Moreover, five polyhedral particle models were established by DEM to study the effect of particle shape on erosion behavior. The numerical calculation results show that the special structure of the bubble cap affords a special serrated erosion wear area. According to the movement process of particles, the erosion wear of the assignment plate is divided into two stages: first a large range of slight erosion wear occurs and then seriously concentrated erosion wear occurs. With the decrease of particle sphericity φ , the erosion wear rate first decreases rapidly and then increases slowly. $\varphi=0.85$ is the critical value of change, and the assignment plate has the lowest erosion wear rate. The simulation studies are helpful for reducing the erosion wear of the assignment plate and improving its service life.

Keywords: CFD–DEM; Erosion wear; Numerical simulation; Gas–solid flow; Particle shape; Assignment plate.

NOMENCLATURE

A_w	surface area	H_v	Vickers hardness
b_1, b_2, b_3, b_4	empirical coefficient	h_0, h_1, h_2, h_3	height in geometric model
C_d	drag coefficient of particle	h_4	
C_s	lift force coefficient	I_p	moment of inertia of the particle
C_{sha}	coefficient of sand sharpness	K	dimensionless constant
d_{ref}	reference diameter	M	mass flow rate of particle
E_r	general erosion rate	m_p	mass of the particle
e_r^1	erosion rate of Finnie model	p_w	flow stress of wall
e_r^2	erosion rate of E/CRC model	$R_{f,p}$	momentum exchange term
e_r^3	erosion rate of Oka model	Re_{sph}	Reynolds number
F_C	contact force	r_0, r_1, r_2	radius in geometric model
F_D	drag force	S_p	surface area of particle
F_L	lift force	S_s	surface area of the sphere
F_M	magnus force	T_p	rotating torque vector acting on the particle surface
$f(\theta)$	function of impact angle	T_c, T_t	contact torque
f_s	sliding friction coefficient	τ_f	stress tensor for fluid phase
u_p	particle velocity	φ	sphericity of particle
u_{ref}	reference velocity	ω_f	fluid rotation velocity
α_f	volume fraction occupied by the fluid	ω_p	particle angular velocity
ε	inter-phase momentum exchange coefficient	∇P	pressure gradient
ρ_f	density of gas-phase		
ρ_w	density of wall		

1. INTRODUCTION

The S Zorb gasoline adsorption desulfurization technology has become the main technique for fluid catalytic cracking gasoline desulfurization in China due to its advantages of high desulfurization rate, low octane loss, low hydrogen consumption, and low energy consumption. According to incomplete statistics, more than 40 sets of S Zorb devices have been produced in China, and a large number of similar devices are being produced. As the core equipment of the device, the adsorbent particles in an S Zorb adsorption desulfurization reactor (hereinafter, the reactor) cause serious erosion wear on the assignment plate due to the transport of gasoline. Once the substrate is damaged, there is high-temperature corrosion risk from hydrogen sulfide. Thus, it is necessary to determine the erosion wear mechanism of the assignment plate. Numerous scholars have conducted studies to determine the formation mechanism of erosion wear and predict the erosion wear process. In the beginning, scholars put forth some wear models pertaining to the causes of wear, which are roughly divided into the following two theoretical explanations: cutting wear theory (Finnie 1962; Finnie 1972; Tilly 1973) and plastic fatigue deformation theory (Bitter 1963a,b; Hutchings 1981). With the advancement of science and experimental technology, wear models in some specific cases have been proposed, which enrich the wear theory. Oka and Yoshida (2005) and Oka *et al.* (2005) conducted erosion experiments on different metal materials. Based on the study of particle impact velocity, impact angle, and particle size, the influence of material hardness and mechanical properties on erosion was deliberated and the prediction equation of impact damage was proposed. Archard (1953) proposed a different hypothesis to explain the wear behavior. He believed that when particles contact the material surface, plastic deformation occurs in the contact area and then the particles continue to move to remove these deformation products, causing wear. He also presented the relation between wear and load. McLaury (1996) proposed a prediction model of slurry erosion and developed the semi-empirical wear model suitable for gas-solid two-phase flow erosion (McLaury 1996; Edwards *et al.* 1998; Wang and Shirazi 2003; Edwards *et al.* 2001; Zhang *et al.* 2007).

Recently, the research of computational fluid dynamics (CFD) in particle erosion has gradually matured. Currently, the CFD-DPM method is employed to simulate the particle flow in a dilute phase, such as spray dryer and coal combustion when the volume fraction of the second phase (particle phase) is low (Patankar and Joseph 2001). For instance, Jafari *et al.* (2015) studied the influence of wall roughness on gas-solid flow erosion in a horizontal annulus under different inner diameter ratios and solid concentrations, and their results showed that wall roughness was positively correlated with the wall erosion rate. Yang *et al.* (2021) determined that the erosion rate exponentially increases with the tensile stress through the impact test of samples containing tensile stress, and they established a new stress

erosion model through machine learning, which successfully predicted the erosion of slurry flow in the elbow under high internal pressure. Moreover, Zolfagharnasab *et al.* (2021) studied the erosion process of square pipe elbows by the CFD-DPM method and analyzed the influence of flow velocity, turbulence intensity, and other factors on erosion. They showed that the erosion rate of a square pipe is lower than that of an ordinary pipe, especially when the particle diameter and flow velocity are large. Liu *et al.* (2020) used a DPM model to study the solid-liquid two-phase erosion behavior of a slotless hydraulic slide valve, revealed the local erosion mechanism, and proposed the accurate calculation method of the orifice plate area under the action of erosion.

Additionally, CFD-DEM has been effectively used when the volume fraction of the second phase is large and the collision and interaction force between particles cannot be ignored. Combining DEM and the rough wall model, Zhang *et al.* (2021) discussed the relation between particle erosion and stress distribution on the target and analyzed the influence of target particle accumulation on the subsequent particle trajectory. Lin *et al.* (2020) used CFD-DEM simulation and determined that the number of particles plays an important role in the erosion on gate valves. Farokhipour *et al.* (2019) observed that with increasing particle mass loads, the efficiency of blocking tees increased compared to that of standard elbows. Xu *et al.* (2016) found that when the particle concentration was low, the coupling method little influenced the erosion prediction, while particle concentration significantly influenced the elbow erosion. Currently, most studies on particle erosion via CFD-DPM and CFD-DEM adopt spherical particles as the particle shapes to simplify the particle-particle and particle-wall collisions. Although researchers at the Erosion/Corrosion Research Center (McLaury 1996; Edwards *et al.* 1998; Wang and Shirazi 2003; Edwards *et al.* 2001; Zhang *et al.* 2007) used shape coefficients to represent particle shapes, empirical formulas have always been limited. Zhou (2022) analyzed the liquid-solid wear characteristics of cylindrical particles in elbow based on experiments and CFD-DEM. It is found that the most serious erosion wear rate is near the exit, followed by the exit near the center of the elbow. Li (2021) studied the influence of particle shape on liquid-solid wear of centrifugal pump blade by CFD-DEM method. Studies have shown that the wear of blades with different particle shapes mainly occurs at the pressure surface length from the blade head to 1/3 of the blade, and at the tail part of the blade. When the sphericity is 0.84, the wear of the volute is the most serious. Zeng *et al.* (2018) simulated the erosion behavior of sulfur particles based on the particle shape and determined that factors, such as impact velocity, angle, and concentration sensitivity, influenced the erosion rate. Thus, particle shape has a certain influence on erosion.

Generally, due to the special throttle structure of an S Zorb reactor, the assignment plate wear caused by it is quite different from the wear of pipes, valves, etc., and the applicability of the commonly used classical empirical wear model needs to be

evaluated. Currently, few studies have analyzed the influence of particle shape on wear and even fewer studies have been conducted using CFD-DEM. Compared with CFD-DPM, CFD-DEM has great advantages in particle generation and tracking, and it is more suitable for wear simulation of non-spherical particles. Therefore, the wear of non-spherical particles in an S Zorb reactor needs to be studied. Herein, based on Fluent 2021 and Altair EDEM 2021, the erosion behavior of particles on the assignment plate of an S Zorb reactor is studied by CFD-DEM. Five polyhedral particle models are established to compare and analyze the relationship between particle shape and erosion wear rate.

2. METHODOLOGIES

2.1 Particle Shape Definition

The DEM method defines the interaction force of particles through Newton's second law, allowing slight deformation and overlap of granular materials in the interaction (Cundall *et al.* 1979). The construction of non-spherical particles mainly comprises the single and composite particle construction methods, and the influence of different particle shapes and modeling methods is also studied (Lu and McDowell 2007; Latham *et al.* 2008; Ferellec and McDowell 2010). Herein, overlapping spheres were used to create complex irregular particle shapes (Vollmari *et al.* 2016). To make the particle model more close to the geometric model, more balls need to be used to express it. Furthermore, to study the influence of particle shape on the erosion wear of the reactor assignment plate, regular polyhedron and spherical models were established based on circular particles with diameters of 100 μm . The detailed parameters are shown in Table 1. Sphericity is used to represent the shape of particles:

$$\varphi = \frac{S_s}{S_p} \quad (1)$$

2.2 Governing Equations

Flow field modeling: The motion of a fluid phase in the presence of a secondary particulate phase is governed by the volume-averaged Navier-Stokes equations for a compressible fluid, which can be written as follows:

$$\frac{\partial(\rho_f \alpha_f)}{\partial t} + \nabla \cdot (\rho_f \alpha_f u_f) = 0 \quad (2)$$

and

$$\begin{aligned} \frac{\partial(\rho_f \alpha_f u_f)}{\partial t} + \nabla \cdot (\rho_f \alpha_f u_f u_f) &= -\alpha_f \nabla p + \\ R_{f,p} + \nabla \cdot (\alpha_f \tau_f) & \end{aligned} \quad (3)$$

It can be solved using a pressure-velocity coupling (PISO), an implicit momentum predictor; a series of pressure solutions; and an explicit velocity correction (Jasak 1996).

Turbulence model: The SST $k-\omega$ turbulence model has advantages in the calculation of near-wall region, wake flow and bypass flow, which is consistent with the flow channel characteristics of S Zorb reactor.

$$\frac{\partial}{\partial t}(\rho k) + \frac{\partial}{\partial x_i}(\rho k u_i) = \frac{\partial}{\partial x_j} \left(\Gamma_k \frac{\partial k}{\partial x_j} \right) + G_k - Y_k \quad (4)$$

$$\begin{aligned} \frac{\partial}{\partial t}(\rho \omega) + \frac{\partial}{\partial x_j}(\rho \omega u_j) &= \frac{\partial}{\partial x_j} \left(\Gamma_\omega \frac{\partial \omega}{\partial x_j} \right) + \\ G_\omega - Y_\omega + D_\omega & \end{aligned} \quad (5)$$

Here, G_k represents the generation of turbulence kinetic energy due to mean velocity gradients. G_ω represents the generation of ω . Γ_k and Γ_ω represent the effective diffusivity of k and ω , respectively. Y_k and Y_ω represent the dissipation of k and ω , respectively, due to turbulence. D_ω represents cross diffusion term.

Discrete particle motion modeling: The force balance of particles is obtained by Newton's first law:

$$m_p \frac{du_p}{dt} = G_p + F_D + F_L + F_M + F_C \quad (6)$$

$$\frac{d\omega_p}{dt} = \frac{T_p}{I_p} \quad (7)$$

Cundall *et al.* (1979) proposed the soft-ball collision model, also known as the linear spring-dashpot model, as shown in Fig. 1. The model simplifies the forces on the collision with high computational efficiency, and it has been widely used in DEM research. In this model, contact force is decomposed into tangential force

Table 1 Parameters of polyhedron particles

	Tetrahedron	Hexahedron	Octahedron	Dodecahedron	Icosahedron
edge length	0.3288	0.1613	0.2071	0.0818	0.1179
φ	0.6711	0.8063	0.8459	0.9102	0.9396
particle model					

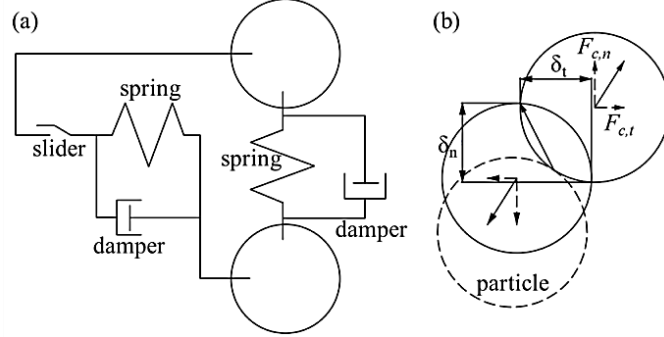


Fig. 1. (a) Constitutive model of the interaction between two particles; (b) normal displacement δ_n and tangential displacement δ_t of particle collision.

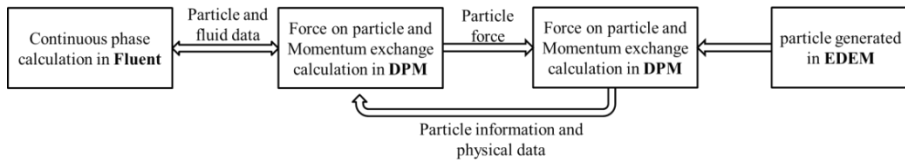


Fig. 2. Coupled calculation flow.

$F_{c,t}$ and normal force $F_{c,n}$:

$$F_{c,n} = -k_n \delta_n - \eta_n v_n \quad (8)$$

$$F_{c,t} = -k_t \delta_t - \eta_t v_t \quad (9)$$

Here, v is the relative velocity between particles; η is the damping coefficient, which is calculated by the recovery coefficient; k is the elastic coefficient; t represents the tangential direction; and n represents the normal direction.

When the following formula is met, sliding friction appears on the contact surface:

$$|F_{c,t}| > f_s |F_{c,n}| \quad (10)$$

At this point,

$$F_{c,t} = -f_s |F_{c,n}| \times \frac{\delta_t}{|\delta_t|} \quad (11)$$

$$T_c = T_t = m \times F_{c,t} \quad (12)$$

The Wen-Yu drag force model (Beetstra et al. 2007) was adopted:

$$F_D = \begin{cases} \frac{150}{18} \frac{(1-\varepsilon)}{\varepsilon^2}, & \varepsilon < 0.8 \\ \frac{Re}{24} C_d (Re) \varepsilon^{-3.65}, & \varepsilon > 0.8 \end{cases} \quad (13)$$

Haider et al. (1989) defined C_d as

$$C_d = \frac{24}{Re_{sph}} \left(1 + b_1 Re_{sph}^{b_2} \right) + \frac{b_3 Re_{sph}}{b_4 + Re_{sph}} \quad (14)$$

where

$$b_1 = \exp(2.3288 - 6.4581\varphi + 2.4486\varphi^2)$$

$$b_2 = 0.0964 + 0.5565\varphi$$

$$b_3 = \exp(4.905 - 13.8944\varphi + 18.4222\varphi^2 - 10.2599\varphi^3)$$

$$b_4 = \exp(1.4681 - 12.2584\varphi - 20.7322\varphi^2 + 15.8855\varphi^3)$$

In addition the velocity near the assignment plate changes significantly; thus, the Saffman's lift force and pressure gradient force are considered. Herein, the density of the solid phase is higher than that of gas phase, so the virtual mass force is not considered.

Saffman's lift force (Saffman 1965) is

$$F_s = 1.615 d_p^2 \left(\frac{\rho_f \mu_f}{|\omega_f|} \right)^{1/2} C_s [(v_f - v_p) \times \omega_f] \quad (15)$$

The pressure gradient force is

$$F_p = \frac{\rho}{\rho_p} \nabla P \quad (16)$$

The CFD and DEM coupling calculation process is shown in Fig. 2.

2.3 Erosion Model

Currently, most classical erosion models are based on empirical formulas. Different from the erosion wear of classical models, such as elbows, the erosion wear of an assignment plate in an S Zorb reactor has been barely studied, and its erosion wear mechanism is unknown. Therefore, the

adaptability of each erosion wear model to the assignment plate needs to be considered.

The Finnie erosion model (Finnie 1962) is defined as follows:

$$e_r^1 = Kf(\alpha) \frac{m_p u_p^2}{P_w} \quad (17)$$

$$f(\alpha) = \begin{cases} \sin 2\alpha - 4\sin^2 \alpha & (\alpha \leq 14.04^\circ) \\ \cos^2 \frac{\alpha}{4} & (\alpha \geq 14.04^\circ) \end{cases} \quad (18)$$

The E/CRC model (El-Behery *et al.* 2010) is defined as follows:

$$e_r^2 = Kf(\alpha) C_{sha} (u_p)^n \quad (19)$$

$$f(\alpha) = \begin{cases} a\alpha^2 + b\alpha & (\alpha \leq 10^\circ) \\ C_1 \cos^2 \alpha \sin(C_2 \alpha) + C_3 \sin^2 \alpha + C_4 & (\alpha \geq 10^\circ) \end{cases} \quad (20)$$

Moreover, the coefficient C_{sha} denotes the sand sharpness and assumes values of 0.2, 0.53, and 1 for rounded, semi-rounded, and sharp grains, respectively. Additionally, a, b, C1, C2, C3, C4, and n are constants.

The Oka erosion model is defined as follows:

$$e_r^3 = K(aHv)^{k_b} f(\theta) \left(\frac{u_p}{u_{ref}} \right)^{k_2} \left(\frac{d_p}{d_{ref}} \right)^{k_3} \quad (21)$$

$$f(\theta) = (\sin \theta)^{n_1} [1 + Hv(1 - \sin \theta)]^{n_2} \quad (22)$$

where a, b, k_1 , k_2 , k_3 , n_1 , and n_2 are constants.

To unify the meaning of erosion, the deformations of the above three models are as follows:

$$E_r^1 = \frac{e_r^1 M \rho_w}{mA_w} = \frac{Kf(\alpha) u_p^2 M \rho_w}{P_w A_w} \quad (23)$$

$$E_r^2 = \frac{e_r^2 M}{A_w} = \frac{Kf(\alpha) F_s(u_p)^n M}{A_w} \quad (24)$$

$$E_r^3 = \frac{KM \rho_w}{A_w} (aHv)^{k_b} f(\theta) \left(\frac{v_p}{v_{ref}} \right)^{k_2} \left(\frac{d_p}{d_{ref}} \right)^{k_3} \quad (25)$$

3. MODEL IMPLEMENTATION

In CFD-DEM calculations, a pressure-based solver is used to solve the flow field. The finite volume method is used to solve the control equation, and the fast discrete scheme is used to solve the momentum and turbulence equations of the polyhedron mesh model. The pressure-velocity coupling is ensured by SIMPLEC method. EDEM 2021 is used to describe solid motion. The two methods are coupled through user defined functions.

3.1 Geometric and mesh

Herein, a distributor on the assignment plate is studied, which comprises a lifting pipe, a bubble

cap, and an assignment plate. Fig. 3 shows the explosion view of the distributor. The right side of the figure displays a geometric model of one-fifth of the distributor, which is actually established. h_0 and δ denote the bubble cap's height and the thickness of the wall, respectively. Additionally, r_0 , r_1 , r_2 are the inner diameter of flow field, bubble cap, and lifting pipe, respectively. Table 2 displays the specific structural parameters. The calculation effect of the whole distributor is realized using a periodic grid, saving computing resources.

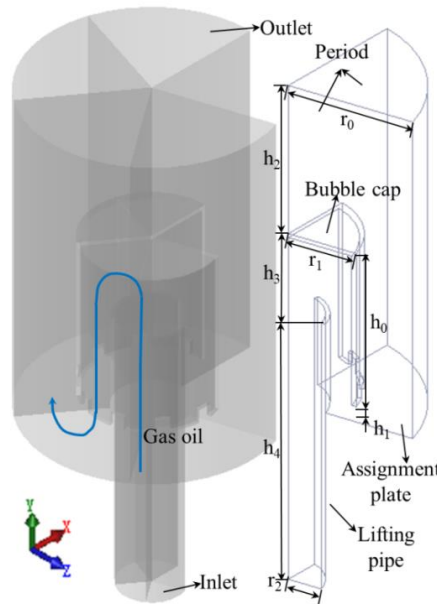


Fig. 3. Explosion view of the distributor.

Table 2 geometrical parameter of the distributor

parameter	mm
h_0	121
r_0	90
r_1	49
r_2	24
δ	3
h_1	12
h_2	117
h_3	60
h_4	210

As mesh generation software, Fluent Meshing performs polyhedral mesh generation for geometric models. Curvature division is used to divide the global fluid domain. In the setting of grid size, the minimum is 1 mm, the maximum is 2 mm, and the grid growth rate is 1.2. The normal angle is 18° , which means dividing the circumference equally into 20 parts. Additionally, proximity is used to increase the mesh density in the thin-wall areas. A progressive mesh is adopted to mesh the boundary with five-layer grids in the radial direction. The height of the first cell is 0.05 mm and the growth factor is 1.2. Taking spherical particles as the standard case, 0.3, 0.5, 0.8, and 1 million

polyhedral grids are meshed, and the sensitivity of the different grids is tested from the erosion wear rate perspective (Fig. 4). The results show that the erosion rate slightly changes with increasing mesh number. When the number of grids is 0.8 million, the erosion rate does not obviously change. For further simulation in the model, the number of grids is set to 0.8 million. The grid diagram is shown in Fig. 5.

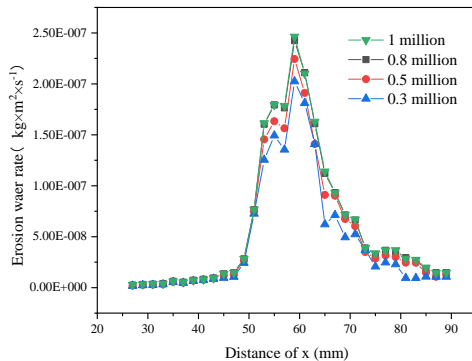


Fig. 4. Erosion rate of extrados with different numbers of meshes

3.2 Boundary Condition

The boundary conditions of a single bubble cap are obtained by simulating the whole flow field of the reactor in advance. For the CFD boundary settings, gasoline is employed as the fluid. The boundary conditions are shown in Table 3. The inlet boundary is set as the velocity inlet, the outlet is set as the pressure outlet, and the operating pressure is set as 2.7 MPa. To ensure the stability of the coupling calculation, the time step of Fluent and EDEM should be integer multiples. The time step of Fluent is set to 1e-5. Table 4 lists the DEM

simulation parameters and material properties employed herein.

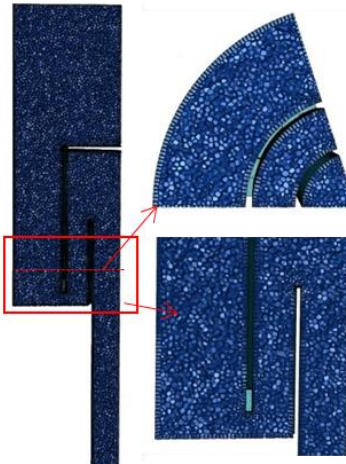


Fig. 5. Meshing diagram.

Table 3 Boundary condition in Fluent

Boundary name	Condition	
Inlet	5m/s	
Outlet	2.7MPa	
Wall-out		
Wall-assignment plate	No slip	reflect
Wall-bubble cap		
Wall-lifting pipe		
Period 1	-	
Period 2	-	

Table 4 DEM Simulation parameters and material properties

Item	Details	Index	Value
Material	Particle	Poisson's ratio [-]	0.23
		Young's modulus [Pa]	2.5e+8
		Density [kg m⁻³]	1906
	Wall	Poisson's ratio [-]	0.3
		Young's modulus [Pa]	1.95e+11
		Density [kg m⁻³]	7960
Interaction	Particle-particle	Coefficient of restitution [-]	0.5
		Coefficient of static friction [-]	0.6
		Coefficient of rolling friction [-]	0.05
	Particle-wall	Coefficient of restitution [-]	0.5
		Coefficient of static friction [-]	0.4
		Coefficient of rolling friction [-]	0.05
Simulator	Time step size	Fixed time step [s]	2e-7
	Simulator grid	Cell size [mm]	1

To simulate the state of particle heaping on the assignment plate, a region fitting to the wall is first embedded in the calculation field, and a particle factory is set on it. The diameter of particle is 100 μm , and the weight of particles is about 0.5912 kg according to the actual particle weight of 1.001 N cm^3 .

3.3 Validation of the Numerical Simulation Method

Taking spherical particles as an example, the applicability of three models for assignment plate wear was compared. In our previous study (Jin et al. 2021), the severe erosion area is usually located on the assignment plate corresponding to the concave part of the bubble cap, which is in the x direction in this example. Therefore, the assignment plate in the x-axis direction is divided into 32 zones ($2 \text{ mm} \times 2 \text{ mm}$) for the comparison of the conformances of the different erosion models.

The calculated wear rates of the three wear models are transformed into dimensionless wear rates. It can be seen from Fig. 6, the erosion rates well agree with one another in terms of both their magnitude and trends.

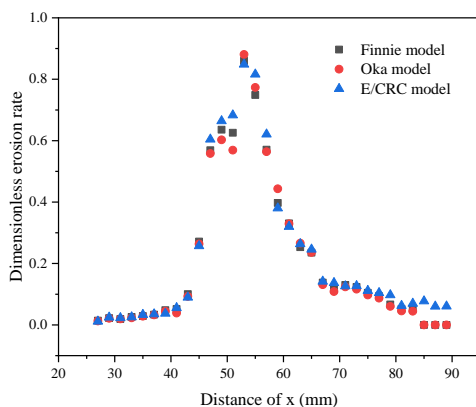


Fig. 6. Comparison of dimensionless erosion rates for the three erosion models.

The standard deviation (S_D) of the dimensionless erosion wear rate under the three models is calculated as 0.2472, 0.2483, and 0.2580 for the Finnie, Oka, and E/CRC models, respectively. This

signifies that the deviation between the Finnie model and the average is the smallest. Therefore, the influence of particle shape on the erosion wear of assignment plate in the reactor was studied by Finnie model.

Figure 7 shows the comparison between the numerical simulation results and the actual failure, and the calculation area is the area shown by the dotted line in Fig. 7 (a). Actual damage and numerical simulations in Fig 7 (a) and (b) show that the severely wear area is partially W-shaped. Outlet of the bubble cap is also serrated, biting each other with serrated areas of severe erosion wear. Comparison of Fig. 7(a) with (b) shows that both erosion wear contour is basically the same. Thus, we consider that the prediction based on the numerical method employed herein is feasible.

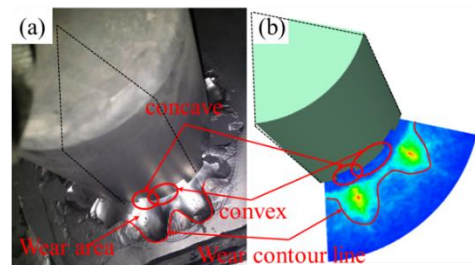


Fig. 7. Comparison of erosion wear morphology; (a) for actual, (b) for simulation.

4. RESULTS AND DISCUSSION

4.1 Simulation Results of the Standard Case

Figure 8 shows the velocity field and the pressure field in the concave and convex parts of the bubble cap. Fig. 8(a), (c), and (e) exhibits the profiles for the concave part, while Fig. 8(b), (d), and (f) exhibits those for the convex part. The flow fields of the two sections are basically the same overall. Gasoline flows upward through the lifting pipe. After the gaseous gasoline flows out of the lifting pipe, the flow rate decreases due to the expansion of the pipe diameter. Then the fluid turns when it encounters the obstruction at the top wall of the bubble cap, and impacts the assignment plate along the channel, and finally flows upward. Eddy flow

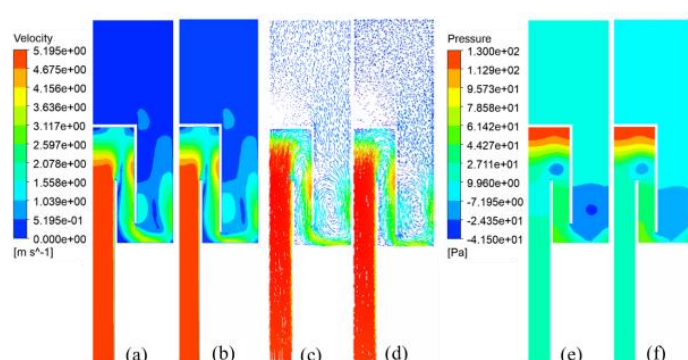


Fig. 8. Velocity field and the pressure field in the concave and convex parts; (a), (b) for velocity contour; (c), (d) for velocity vector; (e) (f) for pressure contour.

forms at the corner, as shown in Fig. 8(c) and (d). Correspondingly, since the pressure of the rotating eddy flow is low, it is shown as a negative pressure area on the pressure contour (Fig. 8(e) and (f)). The difference is that the area of eddy flow at the exit is larger than the exit of the lifting pipe. The outlet at the convex part of the bubble cap is farther than that at the concave part, and the outlet space is smaller. Therefore, compared to the concave parts, the convex outlet flow rate is smaller and the impact angle is smaller. Comparison with Fig. 8(e) and (f) shows that the negative pressure outside the convex outlet is smaller and the eddy flow is weaker than those for the concave part.

Figure 9 shows the distribution of particles at different moments ($t = 0.01, 0.03, 0.05, 0.07, 0.09$ and 0.11 s). When $t = 0.01$ s, gasoline impinges on the granular layer along the bubble cap channel, making the particles near outlet of the bubble cap appear loose. When $t = 0.03$ s, particles near the inner wall of the bubble cap flow out with gasoline from the gap between the bubble cap and assignment plate. When $t = 0.05$ s, with the steering of gasoline, some particles move upward and some particles close to the assignment plate continue to move along the radial direction. Due to the obstruction of the packing particles, gasoline clearly experiences pressure loss. When $t = 0.07$ s, the particles fall back. The falling particles are driven by the gasoline flowing out of the bubble cap, repeating the movement of particles at $t = 0.05$ – 0.07 s. Simultaneously, as the gap between the particles increases, the pressure loss of gasoline decreases and the particles gain more kinetic energy to move upward. Fig. 9(e) and (f) show that the granular layer is gradually uplifted. Fig. 10 shows the erosion wear distribution on the assignment plate in the standard case. The figure shows that the erosion wear on the assignment plate can be roughly divided into two regions. One is the slight erosion region inside the bubble cap, the other is the severe erosion region outside the bubble cap.

The severe erosion region is W-shaped. The convex portion of the serrated erosion region (Area A in Fig. 10) corresponds to the concave portion of the bubble cap. The maximum erosion wear area is a

long strip extending radially outward from the dividing line.

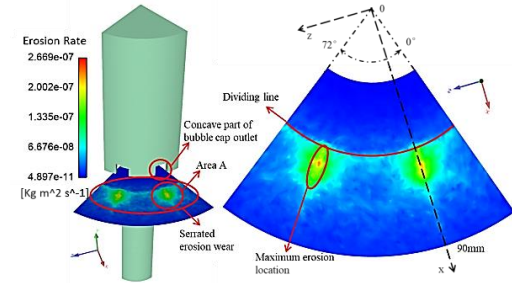


Fig. 10. Erosion wear distribution of the assignment plate for the standard case.

The outlet angles of the two bubble cap concaves are 12° – 24° and 48° – 60° . Fig. 11 shows that the erosion wear in these two intervals is higher than that in the other regions under different x distances, which is consistent with the conclusion obtained in Fig. 10.

Taking area A in Fig. 12 as an example, the erosion wear of assignment plate is divided into two stages according to the impact angle and particle distribution. The first stage is the particle abrasion stage. In this stage, the particles inside and outside the bubble cap differently affect the erosion wear. Fig. 12(a) and (b) show that after the particles in the bubble cap rebound after impacting the assignment plate at a low speed, the particles close to the assignment plate roll or impact the assignment plate at a small angle, causing low-speed and small-angle slight erosion wear on the assignment plate. Simultaneously, these particles form a protective film on the assignment plate. Due to the influence of eddy flow, the particles outside the bubble cap impact the assignment plate downward, but the protective film prevents the particles from impacting the assignment plate and weakens the erosion wear of the assignment plate. The second stage is the erosion stage. In this stage, most of the particles in the bubble cap flow out, gradually decreasing the particles around the assignment plate, and the protective film gradually disappears.

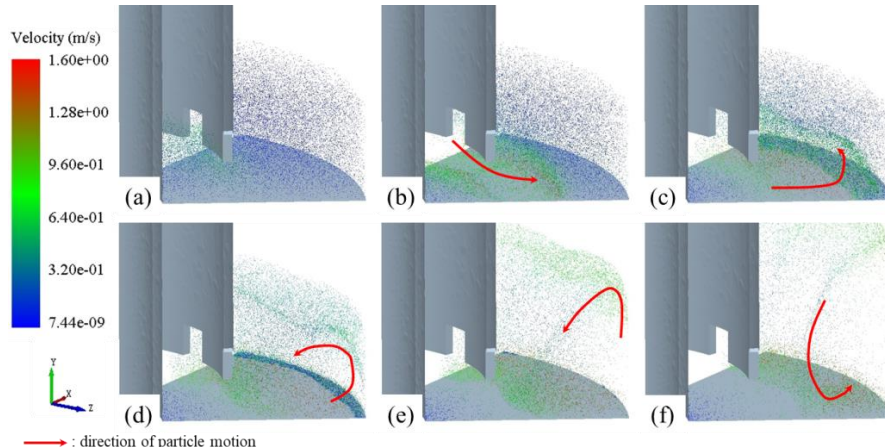


Fig. 9. Particle position and velocity at different times; (a) 0.01s; (b) 0.03s; (c) 0.05s; (d) 0.07s; (e) 0.09s; (f) 0.11s.

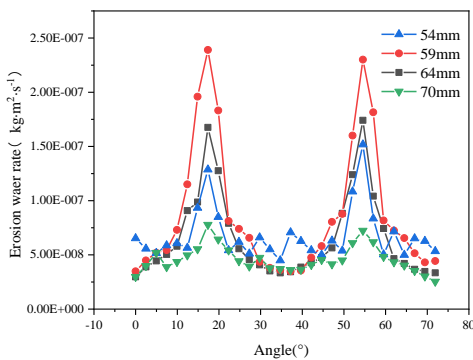


Fig. 11. Curves of erosion wear with angle at different x distances

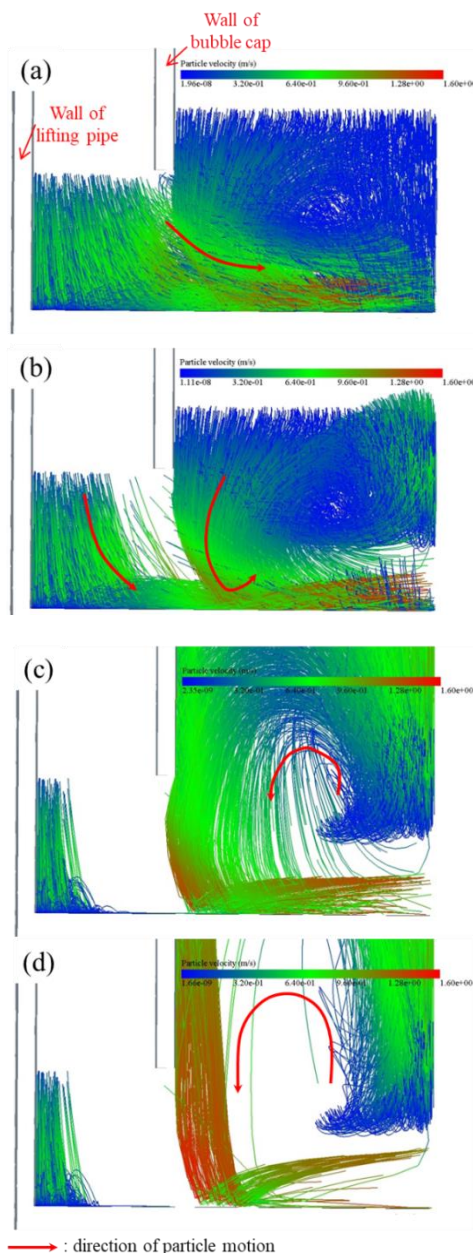


Fig. 12. Particle trajectory at different times: (a) 0.06s; (b) 0.08 s; (c) 0.2 s; (d) 0.3 s.

The falling particles impact the assignment plate at a large angle and high speed, as shown in Fig. 12(c) and (d). Furthermore, with the gradual uplift of the particle layer, the impact angle and impact velocity gradually increase. However, note that with time, the number of particles in the impact assignment plate gradually decreases, the particle distribution becomes concentrated, and the impacted area decreases, which explains the formation of the long strip of the maximum erosion wear region in Fig. 10.

4.2 Effect of Particle Shape on Erosion

It has been shown that the collision concentration is also an important factor affecting the wall wear, and the change of collision concentration will also lead to the change of impact angle and velocity. Collision concentration is the degree of particle collision per unit area. Angular particles exhibit long free paths, which denote that the less surface a particle has and the longer the distance between two adjacent impact points, the fewer collisions occur per unit area. Moreover, the particle surface area decreases with increasing particle sphericity. Therefore, with increasing particle sphericity, the collision concentration increases and the change of the collision concentration becomes slower. After the particles collide with the assignment plate, some particles will roll along with the fluid on the assignment plate, and some particles will spring. Irregular particles have long free transport length and large drag forces; thus, they have large repeated impact velocity. In the first stage of erosion wear, the particles are dense and they roll on the assignment plate or continuously impact the assignment plate at a small angle. The collision concentration becomes the dominant factor of erosion wear, and the particle shape has a great influence. In the second stage, particle density and the probability of secondary impact decrease. At this time, the impact velocity and angle become the dominant factors, while the influence of particle shape is low.

In order to further compare and analyze the influence of particle shape on wear, the polyhedron particles and spherical particles in Table 1 are used for simulation calculation, and φ are 0.671, 0.806, 0.846, 0.910, 0.939 and 1.000, respectively. Fig. 13 shows the assignment plate erosion wear change curve in the x-axis direction for particles of different shapes. The assignment plate erosion wear magnitude within the radius of 51 mm and outside the radius of 69 mm is very small, while the assignment plate erosion wear magnitude within the radius of 51–69 mm is more serious, which is the main research area. In this region, the erosion wear rate first increases and then decreases. The maximum erosion wear of the tetrahedral particles occurs at 61 mm, while that of other particles occurs at 59 mm. Except for spherical particles, the wear curves of all other particles exhibit secondary peak values. The secondary peak values of different particles are different: those for tetrahedral particles appear at 53 mm, while those for the remaining four particles appear at 55 mm. The phenomenon of the two peaks may be due to a secondary collision. Compared with that of other particles, the distance between the two peaks of tetrahedral particles is

larger. Tetrahedral particles have a higher erosion wear rate on the assignment plate than other particles, and icosahedral particles have a higher erosion wear rate than spherical particles, because icosahedral particles have sphericity close to 1 but have more edges and corners.

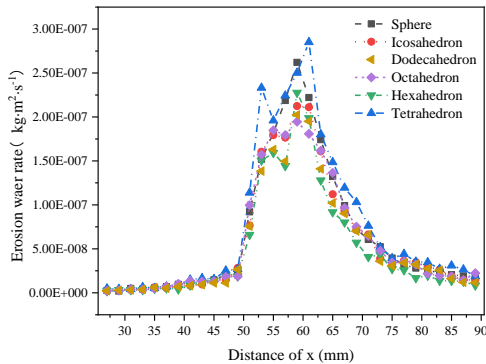


Fig. 13. Erosion wear rate of assignment plate in x axis direction under different particle shapes.

The average erosion wear rate of assignment plate is calculated as an index of quantitative comparison. Taking the average wear rate of spherical particles as a reference, the average wear rates under different particle shapes are dimensionless. According to the dimensionless data, the relationship between the average erosion wear rate of the assignment plate and the particle sphericity φ is obtained by curve regression, as shown in Fig. 14. The error of curve regression is acceptable because R-squared is 0.95593. It can be seen from the figure that the average erosion wear rate of the assignment plate decreases rapidly with the decrease of φ . When φ is less than 0.85, the average erosion wear rate increases slowly with the decrease of φ . If the particle sphericity can be precisely controlled, the erosion wear of the assignment plate can be effectively reduced.

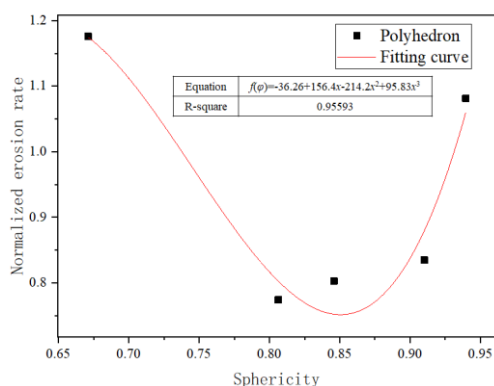


Fig. 14. Regression equation of particle sphericity.

5. CONCLUSION

The erosion behavior of particles on the assignment

plate of S Zorb reactor was studied by CFD-DEM. To verify the accuracy of the model and method, the results of actual working conditions were compared with the actual failure morphology. Combined with the flow field and particle motion characteristics, the particle erosion wear process on the assignment plate was analyzed. Different polyhedron particles were constructed through EDEM, revealing the relationship between the erosion wear of the assignment plate and the particle shape. The following conclusions were reached:

1. The special structure of the bubble cap results in a special serrated erosion wear area. The throttling channel of the concave part is short, resulting in a fast flow rate at the outlet and a large impact range. In contrast, due to the smaller flow field space at the convex part and the longer throttling channel, the range and degree of erosion wear are low.
2. The erosion wear of the assignment plate can be divided into two stages. First, it is easy to have a small angle of continuous collision and rolling, yielding a large range of slight erosion wear for the dense particles. Second, the number of particles is reduced and the particles fall back from high places, causing more severe erosion wear in concentrated areas.
3. The simulation results show that the erosion behaviors are mainly affected by concentration, velocity, and angle of polyhedral particles. With the decrease of φ , the erosion wear rate first decreases rapidly and then increases slowly. $\varphi=0.85$ is the critical value of change, and the assignment plate has the lowest erosion wear rate.

ACKNOWLEDGEMENTS

This work is supported by the National Natural Science Foundation of China (No.52176048, No.51876194, No.U1909216) and General scientific research project of Education Department of Zhejiang Province (Y202045457).

REFERENCES

- Archard, J. F. (1953). Contact and rubbing of flat surfaces. *Applied Physics*, 24, 981-988.
- Beetstra, R., M. Hoef and J. Kuipers (2007). Numerical study of segregation using a new drag force correlation for polydisperse systems derived from lattice-Boltzmann simulations. *Chemical Engineering Science* 62, 246-255.
- Béttiga, R., R. G. Corrêa and J. T. Freire (2010). Scale-up study of spouted beds using computational fluid dynamics. *Canadian Journal of Chemical Engineering* 87(2), 193-203.
- Bitter, J. G. A. (1963a). A study of erosion phenomena: part I. *Wear* 6(1), 5-21.
- Bitter, J. G. A. (1963b). A study of erosion phenomena: part II. *Wear* 1963 6(3), 169-190.
- Brunet, S., D. Mey, G. Pe'rot, C. Bouchy and F. Diehl (2005). On the hydrodesulfurization of

- FCC gasoline: a review. *Applied Catalysis A: General* 278(2), 143-172.
- Cundall, P. A. and O. D. L. Strack (1979). A Discrete Numerical Model for Granular Assemblies. *Geotechnique* 29(1), 47-65.
- Edwards, J. K., B. S. McLaury and S. A. Shirazi (1998). Supplementing a CFD Code with Erosion Prediction Capabilities. In *Proceedings of ASME FEDSM'98: ASME 1998 Fluids Engineering Division Summer Meeting*, Washington DC, June.
- Edwards, J. K., B. S. McLaury and S. A. Shirazi (2001). Modelling Solid Particle Erosion in Elbows and Plugged Tees. *Energy Resources Technology* 123, 277-284.
- El-Behery, S. M., M. H. Hamed, K. A. Ibrahim and M. A. El-Kadi (2010). CFD evaluation of solid particles erosion in curved ducts. *Fluids Engineering* 132, 1-10.
- Farokhipour, A., Z. Mansoori, A. Rasteh, M. A. Rasoulian, M. Saffar-Avval and G. Ahmadi (2019). Study of erosion prediction of turbulent gas-solid flow in plugged tees via CFD-DEM. *Powder Technology* 352, 136-150.
- Ferrellec, J. F. and G. R. McDowell (2010). A method to model realistic particle shape and inertia in DEM. *Granular Matter* 12, 459-467.
- Finnie, I. (1962). ASTM-STP 307 Erosion by solid particles in a fluid stream. In *American Society for Testing and Materials*, in Symposium on Erosion and Cavitation, American.
- Finnie, I. (1972). Some observations on the erosion of ductile metals. *Wear* 19(1), 81-90.
- Haider, A. and O. Levenspiel (1989). Drag Coefficient and Terminal Velocity of Spherical and Nonspherical Particles. *Powder Technology* 58, 63-70.
- Hutchings, I. M. (1981). A model for the erosion of metals by spherical particles at normal incidence. *Wear* 70(3), 269-281.
- Jafaria, M., Z. Mansoorib, M. Saffar Avvala and G. Ahmadic (2015). The effects of wall roughness on erosion rate in gas-solid turbulent annular pipe flow. *Powder Technology* 271, 248-254.
- Jasak, H. (1996). *Error analysis and estimation for the finite volume method with applications to fluid flows*. Ph. D. thesis, Imperial College, London.
- Jin, H. Z., S. Gao, H. Zhao, C. Wang, and G. Ou. (2021). Study on structure optimization of a bubble cap against erosion wear of an S Zorb desulfurization reactor distribution plate. *Part E: Journal of Process Mechanical Engineering* 236, 2, 333-344.
- Latham, J. P., A. Munjiza, X. Garcia, J. Xiang and R. Guises (2008). Three-dimensional particle shape acquisition and use of shape library for DEM and FEM/DEM simulation. *Minerals Engineering*, 21, 797-805.
- Li, J. (2021). *Study on flow and erosion in solid liquid two phase flow centrifugal pump based on CFD-DEM full coupling method*. M.S. thesis, Jiangsu University, Jiangsu, China.
- Lin, Z., X. Sun, T. Yu., Y. Zhang, Y. Li and Z. Zhu (2020). Gas-solid two-phase flow and erosion calculation of gate valve based on the CFD-DEM model. *Powder Technology* 366, 395-407.
- Liu, X., H. Jia, W. Min, Z. Zheng and J. Wang (2020). Erosion behavior and influence of solid particles in hydraulic spool valve without notches. *Engineering Failure Analysis* 108, 104262.
- Lu, M. and G. R. McDowell (2007). The importance of modeling ballast particle shape in the discrete element method. *Granular Matter* 9, 69-80.
- McLaury, B. S. (1996). *Predicting Solid Particle Erosion Resulting From Turbulent Fluctuation in Oilfield Geometries*. Ph.D. thesis, University of Tulsa, Tulsa, OK.
- Oka, Y. I. and T. Yoshida (2005). Practical estimation of erosion damage caused by solid particle impact part 2: mechanical properties of materials directly associated with erosion damage. *Wear* 259, 102-109.
- Oka, Y. I., K. Okamura and T. Yoshida (2005). Practical estimation of erosion damage caused by solid particle impact part 1: effects of impact parameters on a predictive equation. *Wear* 259, 95-101.
- Patankar, N. A. and D. D. Joseph (2001). Modeling and numerical simulation of particulate flows by the Eulerian-Lagrangian approach. *International Journal of Multiphase Flow* 27, 1659-1684.
- Saffman, P. G. (1965). The lift on a small sphere in a slow shear flow. *Fluid Mechanics* 22, 385-400.
- Tilly, G. P. (1973). A two stage mechanism of ductile erosion. *Wear* 23(1), 87-96.
- Ting, J. M. and B. T. Corkum (1992). Computational Laboratory for Discrete Element Geomechanics. *Journal of Computing in Civil Engineering* 6, 129-146.
- Vollmari, K., R. Jasevičius and H. Kruggel-Emden (2016). Experimental and numerical study of fluidization and pressure drop of spherical and non-spherical particles in a model scale fluidized bed. *Powder Technology* 291, 506-521.
- Wang, J. and S. A. Shirazi (2003). A CFD Based Correlation for Erosion Factor for Long-Radius Elbows and Bends. *Energy Resources Technology* 125, 26-34.
- Xu, L., Q. Zhang, J. Zheng and Y. Zhao (2016). Numerical prediction of erosion in elbow based on CFD-DEM simulation. *Powder Technology* 302, 236-246.

- Yang, S., J. Fan, L. Zhang and B. Sun (2021). Performance prediction of erosion in elbows for slurry flow under high internal pressure. *Tribology International* 157, 106879.
- Zeng, D., E. Zhang, Y. Ding, Y. Yi, Q. Xian, G. Yao, H. Zhu and T. Shi (2018). Investigation of erosion behaviors of sulfur-particle-laden gas flow in an elbow via a CFD-DEM coupling method. *Powder Technology* 329, 115-128.
- Zhang, R., X. Zhao, G. Zhao, S. Dong and H. Liu (2021). Analysis of solid particle erosion in direct impact tests using the discrete element method. *Powder Technology* 383, 256-269.
- Zhang, Y., E. P. Reuterfors, B. S. McLaury, S. A. Shirazi and E. F. Rybicki (2007). Comparison of computed and measured particle velocities and erosion in water and air flows. *Wear* 263, 330-338.
- Zhou, J. F. (2022). *Study on liquid-solid flow wear characteristics of non-spherical catalyst particles in tube based on CFD-DEM*. M.S. thesis, Zhejiang Sci-Tech University, Hangzhou, China.
- Zolfagharnasa, M. H., M. Salimi, H. Zolfagharnasa., H. Alimoradi, M. Shams and C. Aghanajafi (2021). A novel numerical investigation of erosion wear over various 90-degree elbow duct section. *Powder Technology* 380, 1-17.